Mechanisms of self-ordering in nonplanar epitaxy of semiconductor nanostructures

G. Biasiol,* A. Gustafsson, K. Leifer, and E. Kapon
Department of Physics, Swiss Federal Institute of Technology Lausanne (EPFL), CH-1015 Lausanne, Switzerland
(Received 31 May 2001; published 25 April 2002)

We have developed an analytic model that describes in detail the establishment of self-ordered profiles during semiconductor epitaxy on corrugated surfaces. Lateral, self-ordered epitaxy derives from surface gradients in the chemical potential due to the nonplanarity of the profile (capillarity). The growth rate variation on the different facets composing the profile determines whether the profile sharpens up at the bottom of the grooves or at the apex of the corrugations. For alloy growth, additional entropy of mixing effects affect the profile shape and composition. The predictions of the model were applied to explain the self-limiting surface profiles obtained by organometallic chemical vapor deposition on $[01\bar{1}]$-oriented grooves. Finally, this model is used to design a variety of low-dimensional quantum-confined nanostructures.

DOI: 10.1103/PhysRevB.65.205306 PACS number(s): 68.65.−k, 68.55.−a, 81.10.Bk, 68.35.Md

I. INTRODUCTION

Low-dimensional semiconductor nanostructures are important both for studies of the physics of low-dimensional systems and for potential applications in novel electronic and optical devices.[1] While two-dimensional semiconductor quantum wells (QW's) are currently fabricated with monolayer control by state-of-the-art epitaxial techniques, production of quantum wires (QWR's) and quantum dots (QD's) requires a lateral control on the structure and its composition, which is difficult to achieve with planar epitaxy.

Different approaches have been adopted in order to obtain lateral patterning of these nanostructures. Methods based on etching and regrowth[2,3] suffer from defect incorporation into the lateral interfaces, since they are not formed *in situ* and are limited in size by the lithographic features. For this reason, much effort has been invested in developing techniques for forming the nanostructures *during* the growth process. This can be achieved if a suitable driving force for *lateral epitaxy* is established on the growing surface, which can order the nanostructures in terms of size, composition, and position. Preferential segregation at steps can produce tilted QWR superlattices (SL's) during growth of a fraction of monolayers on vicinal substrates,[4] while strain fields are the driving force for Stranski-Krastanow growth of strained QD's.[5,6] An alternative approach to this *spontaneous* self-ordering method consists in the creation of a surface template before growth, which acts as a *seed* for the formation of nanostructures.[1] The sites at which self-limiting profiles are formed are determined by the prepatterned profile, while their size and shape depend only on the material and growth conditions. Although this approach introduces an additional processing step, it can result in better nanostructure uniformity, since it overcomes the intrinsic randomness of the nucleation process, exploited in spontaneous self-ordering techniques. Organometallic chemical vapor deposition (OMCVD) and molecular beam epitaxy (MBE) on substrates patterned with V-groove arrays[7–12] and pyramidal recesses[13,14] or masked with SiO_2 stripes[15] have been successfully employed for the formation of uniform arrays of QWR's and QD's.

Despite the remarkable advances in these fabrication techniques in the last decade, the essential principles of the self-ordering mechanisms on nonplanar substrates have remained largely unclear. Experimentally, it has been shown that self-limiting profiles are established thanks to transient diffusion fluxes at the extremal regions of the groove.[9,16] The resulting growth rates thus self-adjust in order to widen or narrow the profile when the deposited material or the growth conditions are changed and, subsequently, stabilize it to a new self-limiting size.[9,16] Such transients, arising for profiles narrower than ~ 50 nm, cannot be accounted for by conventional diffusion models of nonplanar OMCVD (Ref. 17) and MBE (Ref. 18), which take into account lateral diffusion only due to the different crystallographic morphology of the facets composing the profile. In this paper, we will show how self-ordering phenomena, taking place at the 10 nm scale at the top or at the bottom of V-shaped profiles, can be accounted for by capillarity effects, due to the nonplanarity of the surface. Within this model, size-dependent lateral surface diffusion arises due to gradients of the chemical potential, which increase as the profile becomes sharper.[19] Capillarity fluxes modify the intrinsic growth rates on the different facets composing the groove, establishing a self-limiting profile evolution either at the top of the mesas or at the bottom of the grooves, depending on the intrinsic growth rate anisotropy.

In Sec. II we will present the general features of the model, while in Sec. III we will derive the equations describing the different self-ordering phenomena. In Sec. IV we will see how our model can interpret the various self-limiting behaviors observed for different growth techniques and orientations of the corrugations. In Sec. V we will compare quantitatively the predictions of the model with the self-limiting profiles obtained at the bottom of the grooves with low pressure (LP) OMCVD.[9] Finally, we will show in Sec. VI how the model can be used to design and predict the formation of a variety of self-ordered quantum-confined nanostructures.

II. GENERAL EQUATIONS OF THE MODEL

Phenomena of lateral epitaxy can be expressed in terms of gradients of the surface chemical potential μ. Since variations of μ are a measure of the thermodynamical driving

force for epitaxy, they determine surface diffusion fluxes towards regions of lower μ. If the surface properties change only in one dimension (X), μ of the component i of an alloy (considered as an ideal solution[20]) at a growth temperature T is written as[21]

$$\mu_i = \mu_0 + \Omega_0[\sigma_\tau(X)]^2/2E + \Omega_0[\gamma(\theta) + \gamma''(\theta)]\kappa(X) + k_B T \ln x_i(X), \quad (1)$$

where x_i is the component mole fraction. In Eq. (1), the second term is related to the tangential surface stress σ_τ, E being the elastic modulus and Ω_0 the atomic volume,[6] the third one (giving rise to capillarity effects) is due to the surface curvature κ (Ref. 22) and involves the (orientation-dependent) surface free energy $\gamma(\theta)$,[23] and the fourth one is a contribution due to the entropy of mixing.[20]

In the presence of a varying chemical potential, the surface flux j is given by the Nernst-Einstein relation

$$j = -\frac{nD}{k_B T}\frac{\partial \mu}{\partial s}, \quad (2)$$

where n is the surface density of adatoms, D the surface diffusion coefficient, and ds an infinitesimal surface arc length. For one-dimensional profiles, $ds = (dX^2 + dZ^2)^{1/2}$, Z being the coordinate parallel to the growth direction. In the absence of reevaporation (the condition met typically in our growth conditions), the time evolution of the profile $Z = Z(X,t)$ is given by the continuity equation

$$\frac{\partial Z}{\partial t} = R(X) - \Omega_0 \frac{\partial j}{\partial X}, \quad (3)$$

where $R(X) = F(X)/\Omega_0$ is the local growth rate and $F(X)$ is the local growth flux. In principle, the evolution of the growth front can be determined by solving the set of equations (1)–(3) for given initial stress, geometry, and composition surface profiles. Analytical solutions can be found, however, only in particular cases and with suitable approximations. The effects of lateral gradients of stress, for virtually planar surfaces, have been treated in the analysis of the vertical self-organization of Stranski-Krastanow InAs/GaAs islands.[6] Thermal flattening of a nonplanar profile was treated analytically in the 1950s by Mullins for the case of shallow corrugations ($ds \simeq dX$) and above the roughening transition, when the smoothly varying surface free energy can be approximated as a constant.[19] Below the roughening transition, the appearance of low-index, high-symmetry facets (related to cusps in the surface free energy[23]) complicates the diffusion kinetics, whose description still remains somewhat controversial.[24]

The profiles treated here are constituted of artificial, deeply etched grooves,[7–12,16,25] which develop characteristic facets during growth, both at the top and at the bottom of the grooves. The simplified Mullins approach is therefore not valid in our case, since cusps in the surface energy, associated with the faceting of the profile,[23] cannot be treated in the expression (1) of the chemical potential. If the profile is completely faceted, it is more convenient to express the chemical potential on any facet j, with area A_j, and bounded by N other facets, as[23,26]

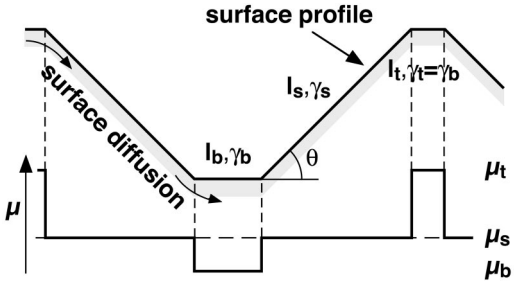

FIG. 1. Top: schematic cross section of a nonplanar profile composed of a top (t) and a bottom (b) parallel facet, separated by a sidewall (s) inclined at an angle θ. Bottom: chemical potential on each facet.

$$\mu_j = \mu_0 + \frac{\Omega_0}{A_j}\sum_{i=1}^{N}(\gamma_i \csc\theta_{ij} - \gamma_j \cot\theta_{ij}) l_i, \quad (4)$$

where θ_{ij} is the angle between facets i and j, l_i is the length of the straight boundary between facet j and i, and γ_i is the surface free energy of facet i. This relation can be derived, in analogy with its continuum equivalent in Eq. (1), by evaluating the change in surface energy associated with a parallel displacement of surface j.[23] Note that the anisotropy of the surface free energy is taken into account without the limitations of Mullins' expression. Here, the local (generally two-dimensional) curvature κ is replaced by the individual contributions l_i/A_j for each facet. Their meaning can be easily understood by considering a rectangular facet with area $A_j = l_1 l_2$: in this case $l_1/A_j = 1/l_2$ is the inverse of the width of facet j in the direction perpendicular to the boundary 1 and is therefore directly related to the facet curvature in this direction.

Several facets develop during growth. For example, in LP OMCVD, growth profiles are composed of a central (100) and two lateral $\{311\}A$ facets at the extremal regions both at the top and at the bottom of the grooves, separated by sidewall planes whose orientation is typically 5°–10° off $\{111\}A$ towards [100].[9] For simplicity, we will, however, take into account in our model a profile composed only of top (t) and bottom (b) parallel facets, separated by a sidewall (s) inclined by an angle θ (see Fig. 1). This will simplify the calculations, since it symmetrizes the boundaries of all facets and allows a more direct interpretation of the role of the parameters involved. Some highlights of a model taking in account the full faceted structure of the profile will be discussed in the Appendix. For the profile of Fig. 1, the chemical potential on the top (t), sidewall (s, inclined by an angle θ), and bottom (b) faces, derived from Eq. (4), assumes the form, respectively,[26]

$$\mu_t = \mu_0 + \frac{\gamma\Omega_0}{l_t},$$

$$\mu_s = \mu_0,$$

$$\mu_b = \mu_0 - \frac{\gamma \Omega_0}{l_b}, \tag{5}$$

where l_t and l_b are the widths of the top and bottom facets, respectively, $\gamma = 2(\gamma_s \csc\theta - \gamma_b \cot\theta)$, and $\gamma_b = \gamma_t$ since they have the same orientation. Note that $\mu_t > \mu_s > \mu_b$, as shown at the bottom of Fig. 1, which sets diffusion fluxes directed towards the bottom region and, consequently, results in an increase (decrease) of the growth rate at the bottom (top).

To determine these resulting growth rates, we have to find a suitable form of the Nernst-Einstein and continuity equations (2) and (3) for the discontinuous μ written above, taking into account also a nonuniform growth flux. Derivatives of the chemical potential and of the diffusion flux should be replaced by discrete variations across neighboring facets. Solving this set of equations will determine the growth rate on each facet, subject to lateral diffusion fluxes due to capillarity effects. We follow the same formalism that Xie *et al.*[6] applied to the case of the vertical self-organization of strained InAs islands. Equation (2) can be discretized by introducing a surface flux from facet *j* to the neighboring facet *i*:

$$j_{ij} = \frac{n_{ij} D_j}{k_B T} \frac{\mu_j - \mu_i}{\lambda_{ij}}, \tag{6}$$

where n_{ij} is the surface density of adatoms at the facets boundary and λ_{ij}, in analogy with the case of strain-dependent chemical potential,[6] is a distance over which the effects of curvature become negligible. We therefore assume $\lambda_{ij} \sim l_t$ and l_b for diffusion to the top and bottom facets, respectively. Note that $D_j / k_B T$ is the adatom surface mobility on the facet *j*, and $(\mu_j - \mu_i)/\lambda_{ij}$ is the average driving force for adatom diffusion. Using Eq. (5), Eq. (6) gives the fluxes at the interfaces between the sidewall and the top and bottom regions, respectively:

$$j_{ts} = \frac{n_{ts} D_s}{k_B T} \frac{\mu_s - \mu_t}{l_t} = -\frac{n_{ts} D_s \Omega_0 \gamma}{k_B T l_t^2} < 0,$$

$$j_{bs} = \frac{n_{bs} D_s}{k_B T} \frac{\mu_s - \mu_b}{l_b} = \frac{n_{bs} D_s \Omega_0 \gamma}{k_B T l_b^2} > 0, \tag{7}$$

where D_s is the diffusion coefficient on the sidewalls.

The growth rates[27] on each facet *j*, surrounded by facets *i* and *k*, are determined by the discretized continuity equation

$$\frac{dZ_j}{dt} = R_j(X) + \frac{\Omega_0}{l_j}(j_{ij} - j_{jk}). \tag{8}$$

The ''deposition'' terms $R_j(X)$ depend generally on the crystallographic orientation of the facet and on the geometry of the surface. For example, in OMCVD the presence of a groove can affect the precursor fluxes supplied from the gas phase,[11,17] while in MBE shadowing effects can be present for off-normal molecular beams.[12] Both effects could in principle reduce the growth rate at the bottom of the grooves. In our structures, however, no growth rate variations are observed across the sidewall planes, in going from the top to the bottom of the mesas. This indicates that a very strong lateral diffusion of precursor species can wash out geometric effects on the gas phase fluxes. This is a peculiarity of LP-OMCVD growth by means of trimethyl group-III precursors, as compared to MBE (where the growth rate on a facet inclined at an angle θ is reduced by a factor $\cos\theta$), or OMCVD with the much more unstable triethylGa and dimethylethylaminealane precursors (where a significant reduction of the growth rates at the bottom of the grooves is observed.[11]) In our case and for MBE in the absence of shadowing effects, we can define therefore the growth rate on each facet as $R_j = R r_j$, where R is the ''nominal'' growth rate on a planar (100) reference sample and r_j an incorporation rate for facet *j*, relative to the nominal one, depending only on the facet orientation. The growth rates at each facet then become

$$\frac{dZ_t}{dt} = R r_t + \frac{2\Omega_0 j_{ts}}{l_t},$$

$$\frac{dZ_s}{dt} = R r_s - \frac{\Omega_0}{l_s}(j_{ts} + j_{bs}),$$

$$\frac{dZ_b}{dt} = R r_b + \frac{2\Omega_0 j_{bs}}{l_b}. \tag{9}$$

In the relations above, we take into account the symmetry of the boundaries limiting the top (bottom) facets, which yields $j_{st} = -j_{ts} (j_{sb} = -j_{bs})$. Note that $j_{ts} < 0$ and $j_{bs} > 0$.

Finally, the lengths of the facets l_t and l_b are related to the growth rates by the geometric relations, valid for a convex and concave profile, respectively:

$$\frac{dl_t}{dt} = p\left(\frac{dZ_s}{dt} - \frac{dZ_t}{dt}\right) = p\left[R\Delta r_{st} + \Omega_0 j_{ts}\left(\frac{1}{l_s} - \frac{2}{l_t}\right) + \Omega_0 \frac{j_{bs}}{l_s}\right],$$

$$\frac{dl_b}{dt} = p\left(\frac{dZ_b}{dt} - \frac{dZ_s}{dt}\right) = p\left[-R\Delta r_{sb} - \Omega_0 j_{bs}\left(\frac{1}{l_s} - \frac{2}{l_b}\right) + \Omega_0 \frac{j_{ts}}{l_s}\right], \tag{10}$$

where the growth rate anisotropy parameters are defined as $\Delta r_{st} = r_s - r_t$ and $\Delta r_{sb} = r_s - r_b$. The geometric factor p depends on the facets intersection angle. To reproduce correctly the proportionality between the growth rate and the facet expansion rate in LP-OMCVD-grown structures, we must take into account that the intersection between the sidewalls and the extremal regions takes place at the $\{311\}A$/sidewall boundary (see Fig. 2 for the bottom region), even if we disregard the faceted nature of the extremal regions. From Fig. 2, we obtain $p = 2/(\tan\theta - \tan\alpha)$, where $\alpha \simeq 25°$ is the angle that the $\{311\}A$ facet forms with the (100) plane and the factor 2 is due to the (symmetric) variations on both sides of the bottom facets. Since typically in our structures $\theta \approx 45°$,[9] we have $p \simeq 3.75$.

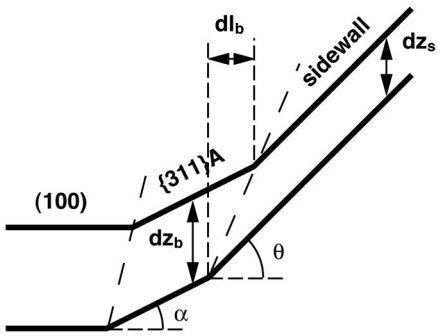

FIG. 2. Schematic illustration showing the geometrical relation between an infinitesimal height variation of the sidewalls dZ_s and of the bottom facets dZ_b, and the corresponding variation in the extension of the bottom region dl_b.

III. PREDICTIONS OF THE MODEL

A. Flattening of the profile in the absence of growth

If no growth flux is present, Eqs. (9) become, with the fluxes described by Eq. (7),

$$\frac{dZ_t}{dt}=-\frac{C}{l_t^3},$$

$$\frac{dZ_s}{dt}=\frac{C}{2l_s}\left(\frac{1}{l_t^2}-\frac{1}{l_b^2}\right),$$

$$\frac{dZ_b}{dt}=\frac{C}{l_b^3}, \tag{11}$$

with

$$C=\frac{2n\Omega_0^2 D_s\gamma}{k_BT},$$

where in this case n is the equilibrium surface density of adatoms.

We will limit our analysis to only the first phases of the relaxation process, when the evolving contour is still shape preserving and the sidewall regions are still extending over the majority of the grooved profile: $l_s \gg l_t, l_b$. This implies that, in Eq. (11), $|dZ_s/dt| \ll dZ_t/dt$, dZ_b/dt, and therefore Eqs. (10) become

$$\frac{dl_{b,t}}{dt}\cong\frac{Cp}{l_{b,t}^3},$$

for the top and bottom facets, respectively. These equations can be integrated, yielding

$$l_t(t)=l_{t0}(1+t/\tau_t)^{1/4},\quad \tau_t=l_{t0}^4/4Cp,$$

$$l_b(t)=l_{b0}(1+t/\tau_b)^{1/4},\quad \tau_b=l_{b0}^4/4Cp, \tag{12}$$

where $l_{b,t0}=l_{b,t}(t=0)$. These expressions show that both the top and bottom of the profile tend to widen *ad infinitum* in the absence of a growth flux. Therefore, as expected qualitatively from Mullins' analysis,[19] nonplanar self-limiting profiles cannot be established in the presence of surface diffusion alone. This monotonic expansion of the groove extrema will eventually lead to its planarization, although with a different time dependence than the one predicted by Eq. (12), which is valid only for the initial stages of surface relaxation.

B. Self-limiting profiles during epitaxial growth

In the presence of a growth flux, the quantities n_{ts} and n_{bs} can be determined by applying the procedure of Ref. 6 for the sidewalls. For our geometry, however (where we are interested in the limit $l_s \gg l_{t,b}$), these densities can be approximated as $n_{ts,bs}\simeq Rr_s\tau_s/\Omega_0$, where τ_s is the lifetime for adatom incorporation on the sidewalls (adatom desorption can be neglected under our growth conditions). With this approximation, the set of equations (9) becomes

$$\frac{dZ_t}{dt}=R\left(r_t-r_s\frac{C}{l_t^3}\right),$$

$$\frac{dZ_s}{dt}=Rr_s\left[1+\frac{C}{2l_s}\left(\frac{1}{l_t^2}-\frac{1}{l_b^2}\right)\right],$$

$$\frac{dZ_b}{dt}=R\left(r_b+r_s\frac{C}{l_b^3}\right), \tag{13}$$

with

$$C=\frac{2\Omega_0 L_s^2\gamma}{k_BT}$$

and $L_s\equiv(D_s\tau_s)^{1/2}$ being the adatom diffusion length. With the approximation $l_s \gg l_{b,t}$ we can neglect the capillarity effects on the sidewalls and assume $dZ_s/dt\simeq Rr_s$. Equations (13) show that capillarity tends to direct adatoms to the concave bottom region and to drive them away from the convex top region.

According to Eq. (10), self-limiting profiles are achieved when the growth rates on two neighboring facets are equal. Due to the crystallographic equivalence between the top and bottom regions, we can assume $r_t=r_b$ and hence, $\Delta r_{st}=\Delta r_{sb}\equiv\Delta r$. Therefore, equalization of the growth rates on two adjacent facets is possible either at the bottom of the groove or at the top of the mesa, depending of the sign of the growth rate anisotropy Δr. If $\Delta r>0$, self-limiting growth is obtained *at the bottom of the groove*, while if $\Delta r<0$, self-limiting growth is obtained *at the apex of the corrugations*. In either case, the self-limiting widths $l_{b,t}^{sl}$ are obtained by setting $dl_{b,t}/dt=0$ in Eq. (10):

$$l_{b,t}^{sl}=\left(C\frac{r_s}{|\Delta r|}\right)^{1/3}. \tag{14}$$

Therefore, a self-limiting evolution of a concave (convex) profile is possible *only* if the growth rate on the surrounding facets, in the absence of the positive (negative) capillarity, is larger (smaller) than that at the curved region in question.

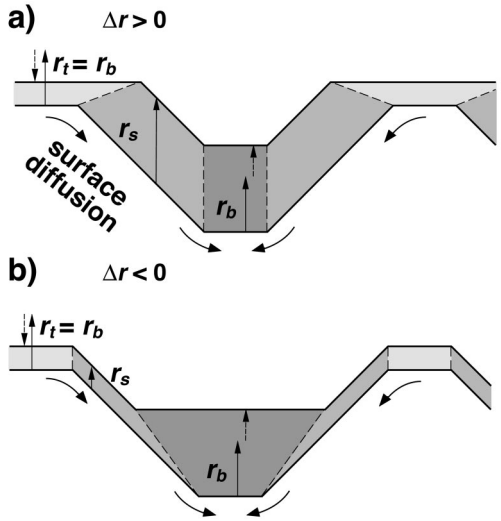

FIG. 3. a) Schematic evolution of a V-grooved profile for a positive growth rate anisotropy (see text), yielding self-limiting propagation of the bottom facet, thanks to capillarity effects. b) The same for a negative growth rate anisotropy, yielding self-limiting propagation of the top facet.

The two different situations are sketched in Fig. 3. Part (a) describes the profile evolution for the case $\Delta r>0$: the additional, capillarity-induced growth rate at the bottom facet balances exactly r_s, yielding self-limiting growth in this region. At the top, capillarity decreases further the growth rate on this facet, which therefore expands indefinitely, leading to a planarization of the groove. Part (b) describes the situation for $\Delta r<0$, where capillarity can compensate for the growth rate anisotropy at the top, while the bottom facet will always grow faster than the sidewalls, thus expanding and leading eventually to planarization.

C. Evolution towards self-limiting profiles

From relations (13) and (14), the GaAs growth rate at the bottom of the groove (relative to the nominal one) can be written for $\Delta r>0$ and $\Delta r<0$, respectively, as

$$\frac{dZ_b}{dZ_n}=r_b+\Delta r\left(\frac{l_b^{sl}}{l_b}\right)^3, \tag{15a}$$

$$\frac{dZ_t}{dZ_n}=r_b+\Delta r\left(\frac{l_t^{sl}}{l_t}\right)^3, \tag{15b}$$

where $dZ_n=R\ dt$. For the self-limiting bottom region, Eq. (15a) states that the bottom growth rate (i) diverges for $l_b \ll l_b^{sl}$, since in this limit the (negative) bottom chemical potential and the related surface diffusion fluxes diverge [see Eqs. (5) and (7)]; (ii) approaches r_s for $l_b \to l_b^{sl}$, establishing a uniform growth rate across the bottom faceted profile; and (iii) approaches r_b for $l_b \gg l_b^{sl}$, since in this limit the capillarity (and entropy of mixing) effects become negligible [see Eqs. (5) and (7)].

The self-limiting behavior at the top, described by Eq. (15b), is similar. However, note that when l_t is sufficiently small $[l_t<l_t^{sl}(-\Delta r/r_b)^{1/3}]$ this equation would predict an overall *negative* growth rate at the top, due to the dominance of negative capillarity effects. This situation could occur, for example, in GaAs growth on extremely sharp, etched ridges of a GaAs substrate. On the other hand, this equation cannot predict correctly the profile evolution for the first stages of GaAs/AlGaAs heteroepitaxy in the case $l_t<l_t^{sl}(-\Delta r/r_b)^{1/3}$, since a negative growth rate would in this case involve capillarity-induced diffusion of the different underlying material, with lower diffusion length and l_t^{sl}.

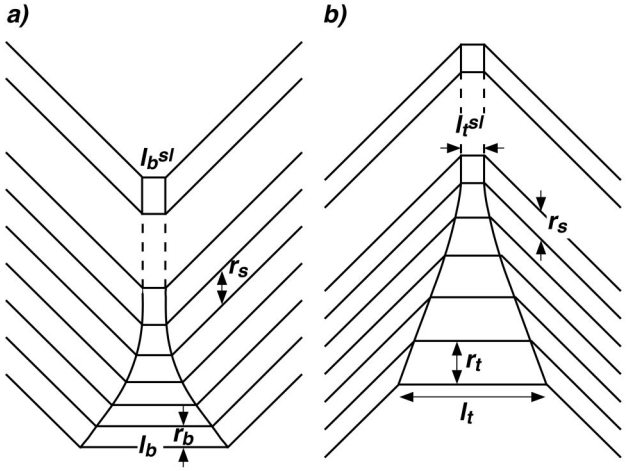

FIG. 4. (a) Self-limiting evolution of the bottom profile, for the case $\Delta r>0$ and $l_b>l_b^{sl}$. (b) The same for the top profile, with $\Delta r<0$ and $l_t>l_t^{sl}$.

From Eq. (15), the self-limiting evolution of the bottom or top profiles (10) can be written as a function of the nominal growth thickness:

$$\frac{dl_b}{dZ_n}=p\Delta r\left[\left(\frac{l_b^{sl}}{l_b}\right)^3-1\right] \quad (\Delta r>0), \tag{16a}$$

$$\frac{dl_t}{dZ_n}=-p\Delta r\left[\left(\frac{l_t^{sl}}{l_t}\right)^3-1\right] \quad (\Delta r<0). \tag{16b}$$

Consistently with the analysis of the bottom growth rates, relations (16) show that l_b and l_t tend to expand (contract) when their size is smaller (larger) than their self-limiting one. The recovery rates increase as these deviations become bigger. Therefore, l_b and l_t will always tend towards their self-limiting values, defined only by the material and the growth conditions. In particular, if the initial width of a bottom facet is much narrower than the self-limiting one, a rapid expansion of this facet will occur during the initial stages of growth. Conversely, if the initial profile is much wider than the self-limiting one, then the profile will contract initially at a rate $\propto|\Delta r|$ (i.e., the *intrinsic* growth rate anisotropy), since in this limit capillarity effects are negligible. The bottom and top profile evolutions in this latter case are shown schematically in Figs. 4(a) and 4(b), respectively.

D. Self-ordering of alloys: Entropic contributions

OMCVD growth of $Al_xGa_{1-x}As$ alloys on V-grooved surfaces results in the formation of a self-limiting, Ga-rich *vertical quantum well* at the bottom of the corrugations.[28] This compositional modulation can be easily understood in terms of the stronger surface diffusion of Ga, with respect to Al,[29] which gives rise to larger capillarity fluxes of Ga towards the bottom for a given surface profile [see Eq. (7)]. The partial compositional ordering due to capillarity results in a decrease of the surface entropy of mixing, with respect to the one for a uniform composition.[20] Entropy of mixing effects cause an increase of the bottom chemical potential for Ga adatoms and a decrease of the one for Al adatoms, therefore hindering Ga diffusion and enhancing Al diffusion towards the bottom. The resulting partial growth rates of AlAs and GaAs can be written as

$$\frac{dZ_b^A}{dt}=xR\left[r_b^A+\Delta r^A\left(\frac{l_{b,A}^{sl}}{l_b}\right)^3+2\left(\frac{L_s^A}{l_b}\right)^2\ln(x(1-k)+k)\right],$$

$$\frac{dZ_b^G}{dt}=(1-x)R\left[r_b^G+\Delta r^G\left(\frac{l_{b,G}^{sl}}{l_b}\right)^3+2\left(\frac{L_s^G}{l_b}\right)^2\ln\frac{x(1-k)+k}{k}\right],$$

with indexes A referring to AlAs and G referring to GaAs. The last terms in both equations are the entropy of mixing contributions, where the bottom Al mole fraction x_b has been expressed as $x_b=x/[x(1-k)+k]$. This relation is typical of diffusion models involving enthalpic and entropic contributions that can be derived empirically by assuming an overall local Ga flux at the bottom (growth plus lateral) being enhanced by a factor $k>1$, with respect to that of Al.[30] The alloy self-limiting width of the bottom facet, resulting from the equalization of the bottom and sidewalls growth rates, is the solution of the equation

$$\frac{a}{(l_b^{sl})^3}+\frac{b}{(l_b^{sl})^2}=\Delta r(x), \tag{17}$$

with

$$a=x\Delta r^A(l_{b,A}^{sl})^3+(1-x)\Delta r^G(l_{b,G}^{sl})^3,$$

$$b=2\left\{x(L_s^A)^2\ln[x(1-k)+k]+(1-x)\times(L_s^G)^2\ln\frac{x(1-k)+k}{k}\right\},$$

$$\Delta r(x)=x\Delta r^A+(1-x)\Delta r^G.$$

The self-limiting profile of an alloy is therefore expressed as the result of the interplay among capillarity (a), entropy of mixing (b), and growth rate anisotropy $[\Delta r(x)]$.

The evolution of the alloy growth rate and facet width at the bottom are given by, respectively,

$$\frac{dZ_b}{dZ_n}=r_b(x)+\Delta r(x)\left(\frac{l_b^{sl}}{l_b}\right)^3+\frac{b}{l_b^3}(l_b-l_b^{sl}), \tag{18a}$$

$$\frac{dl_b}{dZ_n}=p\left\{\Delta r(x)\left[\left(\frac{l_b^{sl}}{l_b}\right)^3-1\right]+\frac{b}{l_b^3}(l_b-l_b^{sl})\right\}, \tag{18b}$$

which are identical to Eqs. (15a) and (16a) for a binary III-V compound, except for the entropy-related term [proportional to the b term in Eq. (17)]. Note that the qualitative behavior of the profiles (Sec. III C) remains valid also in the case of alloy growth.

IV. INTERPRETATION OF EXPERIMENTAL GROWTH BEHAVIORS

The observed behavior of nonplanar epitaxy depends critically on the growth technique and on the orientation of the corrugations. OMCVD on GaAs (100) substrates patterned with $[01\bar{1}]$-oriented grooves gives rise to straight sidewall planes, misoriented about 5°–10° from $\{111\}A$ towards (100), whose orientation is preserved during growth.[9] Their uniform growth rate is generally 20%–25% higher than that on the facets at the bottom and apex of the corrugations, probably due to the high density of steps forming on these high-index planes. In agreement with our model, this positive growth rate anisotropy yields a self-limiting evolution of the bottom growth front, while the top region expands until planarization is accomplished [see Fig. 3(a)].[9] Uniform, vertical arrays of (In)GaAs/(Al)GaAs QWR's have been successfully grown at the bottom of the grooves with this technique.[7–11] Notice that a similar self-limiting formation of QWR's at the bottom of V grooves can be obtained as well with OMCVD on (100) substrates patterned with $[01\bar{1}]$-oriented SiO_2 stripes.[31] On the other hand, MBE on $[011]$ grooves exposes exactly oriented $\{111\}B$ sidewalls, whose growth rate is much smaller than on the extremal (100) facets.[16] In this case, the negative growth rate anisotropy causes a narrowing of the top of the mesas and can balance capillarity fluxes in this region, while the bottom does not present any self-limiting behavior [see Fig. 3(b)]. With this technique, self-ordered QWR's have been grown on the top facets.[12] Some examples of OMCVD growth on GaAs (100) patterned with $[011]$-oriented SiO_2 stripes have shown a similar behavior, with the formation of exactly oriented $\{111\}B$ sidewalls;[15] therefore, the groove orientation is a critical parameter in defining the growth rate anisotropy and consequently the self-ordering behavior. On the other hand, MBE on $[01\bar{1}]$-oriented grooves generally does not exhibit clear self-ordering behavior either at the top or at the bottom of the corrugations, probably due to the instability of the sidewall planes. AlAs growth is an exception, yielding a resharpening behavior at the bottom of the grooves.[25]

To compare in more detail the predictions of the model for the experimental profiles, we will concentrate on self-limiting $GaAs/Al_xGa_{1-x}As$ bottom profiles grown by low-pressure (20 mbar) OMCVD on GaAs (100) substrates patterned with $[01\bar{1}]$-oriented V grooves. Growth details can be found in Ref. 9.

V. APPLICATION OF THE MODEL TO NONPLANAR OMCVD GROWTH

A. $Al_xGa_{1-x}As$ profiles: Dependence on the composition

Figure 5(a) shows a series of dark-field transmission electron microscopy (TEM) cross sections of self-limiting $Al_xGa_{1-x}As$ layers grown at 700 °C, with x increasing between 0.30 and 0.75. Nominally 5-nm-thick GaAs markers were inserted to measure the self-limiting $Al_xGa_{1-x}As$ profile width. The images show that the bottom profile becomes sharper as the Al mole fraction is increased, while the angle between the sidewalls slightly decreases. Note the faceted nature of the profile, composed of a central (100) plane separated from the high-index sidewalls by two $\{311\}A$ planes (see third image from top). The recovery of the $Al_xGa_{1-x}As$ self-limiting profile after its broadening during GaAs growth is accompanied by the approaching of the three vertical quantum well (VQW) branches that correspond to each bottom facet.[28] In Fig. 5(b) we show the dependence of the self-limiting width of the bottom profile l_b^{sl} [$(100)+\{311\}A$ width; see arrow in Fig. 5(a)] on the composition for a series of different samples grown at 700 °C. Since the nominal growth rates R are different for different Al compositions and our model implies a dependence of the profile width on $R^{-1/3}$ (see below), we have normalized the values of l_b^{sl} to the cubic root of the alloy growth rates, relative to the GaAs one. Since the maximum growth rate was 0.53 nm/s and the minimum (for GaAs) was 0.25 nm/s, this normalization yields a correction factor of at most 1.25. The data show that the profile sharpens up by a factor of about 15 upon going from GaAs to AlAs.

To model the evolution of the bottom profile with x, we apply Eq. (17), which takes into account independent Ga and Al adatom diffusion, as well as the effects of the entropy of mixing. Note that, since $(L_s^G)^2 \gg (L_s^A)^2$, the AlAs term of b is negligible for the entire composition range with respect to the GaAs one. We will therefore neglect the AlAs entropy term, thus ascribing any entropy-related compositional variations in the VQW to *Ga diffusion* away from the bottom. In Fig. 5(b) we fit the experimental data with the solution of Eq. (17) (solid line). In the fit, we left L_s^G as the only free parameter, as we inferred the other quantities from the experiments: $k=1.81\pm0.05$,[30] $l_{b,G}^{sl}=129\pm3$ nm, $l_{b,A}^{sl}=9.1\pm0.1$ nm, and $\Delta r^G=0.22\pm0.05$. We have no reliable estimate for Δr^A at our disposal; however the fit is very insensitive to this parameter: by changing Δr^A from 0 to 1, the corresponding best fit of L_s^G varied only by about 4%, without affecting the quality of the fit. The main source of uncertainty in the fit is the error in Δr^G, which causes a $\sim 10\%$ error in the determination of L_s^G: $L_s^G=175\pm20$ nm. The Ga diffusion length on the sidewalls is therefore smaller than on the (100) ridges (estimated to be $\geqslant 0.5$ μm at 700 °C by atomic force microscopy measurements). This conclusion is consistent with the fact that the sidewalls consist of high-index planes, with a higher density of steps and kinks, and hence a better incorporation efficiency than the monolayer-smooth (100) facets.

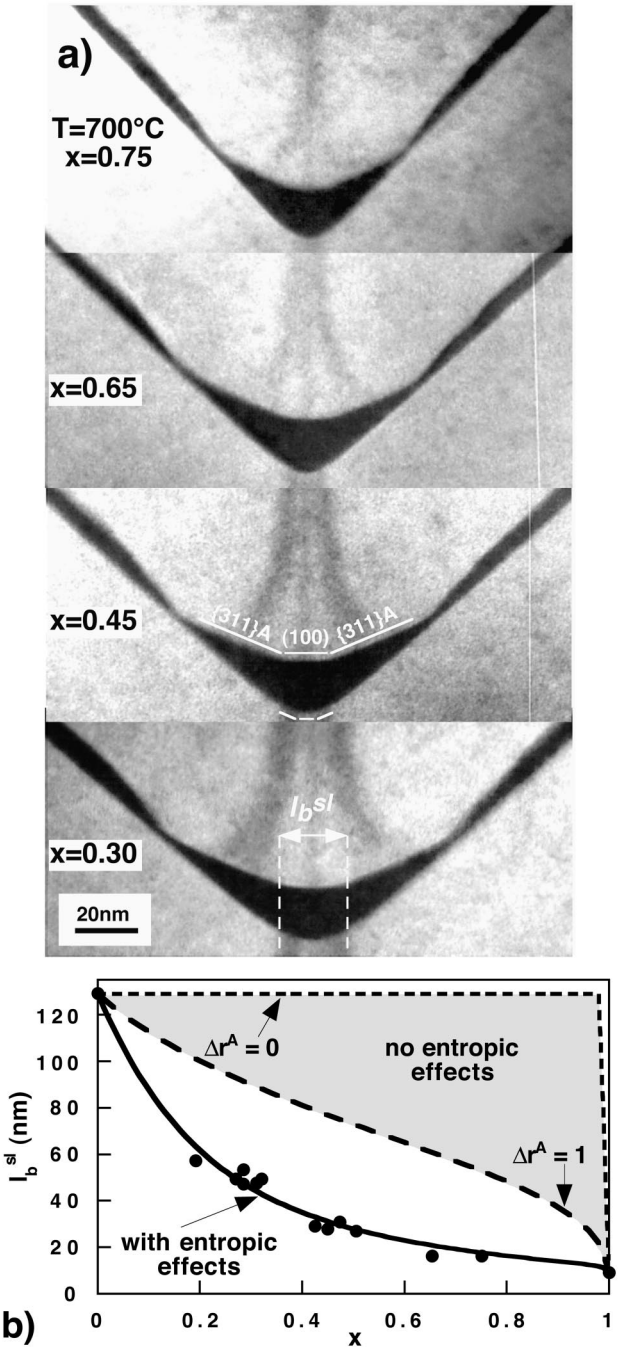

FIG. 5. (a) Dark field TEM cross sections of a series of four self-limiting $Al_xGa_{1-x}As$ layers, grown by low-pressure OMCVD at 700 °C, with x ranging between 0.30 and 0.75, where nominally 5-nm-thick GaAs markers were inserted. (b) Measured self-limiting width of the bottom profile, as a function of x for 700 °C. The solid line is a fit to the data, with the function defined in Eq. (17). Long-dashed and short-dashed lines, delimiting the shaded region, represent the dependence of l_b^{sl} on x neglecting the entropy of mixing effects and setting $\Delta r_G=0.22$ and $\Delta r_A=1$ or $\Delta r^A \to 0$, respectively (see text for details).

Without entropy of mixing effects, the solution of Eq. (17) would reduce to

$$l_b^{sl} = \left(\frac{a}{\Delta r(x)} \right)^{1/3} = \left(\frac{x(\Delta r^A/\Delta r^G)(l_{b,A}^{sl})^3 + (1-x)(l_{b,G}^{sl})^3}{x(\Delta r^A/\Delta r^G) + (1-x)} \right)^{1/3}.$$

We indicated with a shaded region in Fig. 5(b) how l_b^{sl} would depend on x, according to the expression above, setting the limiting values $\Delta r^G = 0.22$ and $\Delta r^A = 1$ (long-dashed line) or $\Delta r^A \to 0$ (short-dashed line). It is clear that the experimental results cannot be reproduced with this simplification (unless one takes unphysically large values of the ratio $\Delta r^A/\Delta r^G$ of the order of 60).

B. $Al_xGa_{1-x}As$ profiles: Dependence on the growth temperature

Figure 6(a) shows a series of dark-field TEM cross sections of self-limiting $Al_{0.45}Ga_{0.55}As$ layers, grown at different temperatures (600–765 °C). Nominally 8.7-nm-thick GaAs markers were inserted to measure the self-limiting $Al_{0.45}Ga_{0.55}As$ profile width. Reducing the growth temperature has qualitatively the same effect of increasing the Al mole fraction, i.e., a sharpening of the profile and a slight reduction in the angle between the sidewalls. The profile sharpening can be understood in both cases as due to the reduction of the diffusion length [see Eq. (14)].

Equation (14), valid for GaAs, can be rewritten as

$$l_b^{sl} = \left(\frac{r_s}{\Delta r} \frac{2\Omega_0 \gamma}{k_B T} D_s \tau_s \right)^{1/3}, \tag{19}$$

with D_s of the Arrhenius form $D_s = D_{s0}\exp(-E_B/k_BT)$, E_B being the activation energy for diffusion. The parameter τ_s can be approximated as the average time passing between the arrival of two adatoms at the same site; thus, $\tau_s = 1/R$ (if R is expressed in ML/s) (Ref. 32) can be considered as a temperature-independent quantity. Therefore, the temperature dependence of l_b^{sl} has an Arrhenius form $\exp(-E_B/3k_BT)$, Δr being virtually constant in the temperature range considered.[33] For $Al_xGa_{1-x}As$, the temperature dependence of l_b^{sl}, given by Eq. (17), is more complicated and comes essentially from the Arrhenius form of $l_{b,A}^{sl}$, $l_{b,G}^{sl}$, L_s^A, and L_s^G.

The profile width is characterized by the length of the (100) and $\{311\}A$ facets. However, when the profile becomes too narrow, these facets are not easily distinguishable. In this case, it is useful to approximate the profile with a hyperbola tangent to the bottom and sidewall facets [see the third profile from top in Fig. 6(a)].[34] The growth front is therefore fully identified by the radius of curvature ρ at the bottom of the hyperbola [that is, proportional to the (100)+{311}A facet length] and by the asymptotic angle θ between the sidewalls and the horizontal. It can be shown analytically that, except for a geometrical proportionality factor, the equations describing the self-limiting profiles and the profile evolution are the same, whether expressed in terms of l_b or ρ.

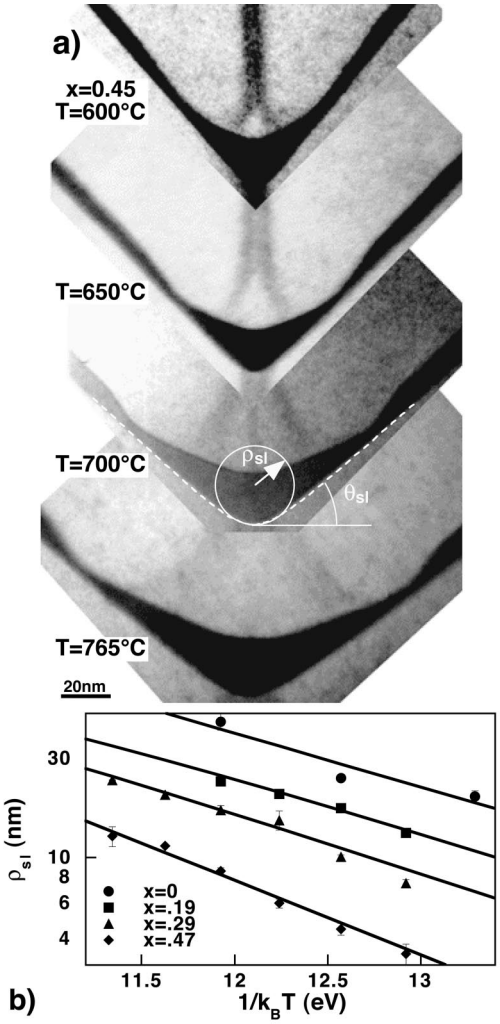

FIG. 6. (a) TEM cross sections of a series of four self-limiting $Al_{0.45}Ga_{0.55}As$ layers, grown at temperatures ranging between 600 and 765 °C, where nominally 8.7-nm-thick GaAs markers were inserted. The dashed line represents a hyperbolic fit of the groove profile. (b) Arrhenius plot of ρ_{sl}, for AlGaAs alloys with composition ranging between $x=0$ and $x=0.47$. Solid lines are fits of the experimental data with Eq. (19) (GaAs) or Eq. (17) ($Al_xGa_{1-x}As$).

We have examined the temperature dependence of the self-limiting profiles for $Al_xGa_{1-x}As$ alloys for $0<x<0.45$. Figure 6(b) shows Arrhenius plots of ρ_{sl} for $x=0$, 0.19, 0.29, and 0.45 for growth temperatures ranging from 600 to 750 °C. The Arrhenius fit for GaAs gives $E_B^G = 1.9 \pm 0.3$ eV. The GaAs behavior can be plugged into Eq. (17) to fit the $Al_xGa_{1-x}As$ profiles, as a function of L_s^G only. As before, we have assumed $(L_s^G)^2 \gg (L_s^A)^2$, fixed $\Delta r^G = 0.22 \pm 0.05$ (this value does not change appreciably with T, in the range considered), and verified the insensitivity of the fit to the value of Δr^A. Least-squares fits of the $Al_xGa_{1-x}As$ profiles, shown in Fig. 6(b), are practically indistinguishable from Arrhenius laws and yield $E_B^A = 2.3 \pm 0.2$ eV, consistently for the three

compositions. This higher energy is consistent with stronger Al-As bonds with respect to Ga-As ones.[29] A more quantitative discussion of these values, in comparison with what has been found on (100) surfaces, is, however, not useful due to the wide range of results obtained on this orientation.[29]

Finally, we can estimate the order of magnitude of L_s^G and L_s^A. By using Eq. (19) with $\gamma \approx 50$ meV/Å^2,[35], $r_s \sim 1$, $\Delta r \sim 0.2$, and, for example, the measured values of l_b^{sl} in GaAs and AlAs layers at 700 °C (~ 100 nm and ~ 10 nm, respectively), we obtain $L_s^G \approx 150$–200 nm and $L_s^A \approx 5$ nm. This value of L_s^G agrees well with the estimate given in the previous section.

C. Effects of the growth rate

By decreasing the growth rate R, the self-limiting profile should expand (until it becomes planar in the absence of growth—see Sec. III A) since effects of diffusion towards the bottom of the groove become increasingly dominant with respect to the effects of growth rate anisotropy. We have verified this hypothesis on self-limiting GaAs profiles, with growth rates ranging between 0.036 and 0.370 nm/s. Two series of layers were grown at 650 and 700 °C, respectively. The GaAs layers were separated by 10-nm-thick AlGaAs markers, grown at 0.5 nm/s. As verified in previous studies,[36] all the GaAs layers were thick enough to ensure the achievement of a self-limiting GaAs profile at their top interface. Figure 7(a) is a TEM cross section of the series grown at 650 °C. The growth rates increase progressively from layer 1 to 4. It can be seen from the upper interface of the GaAs layers and the corresponding AlGaAs markers that the profile narrows down as R increases. Figure 7(b) shows ρ_{sl} for $T = 650$ °C (circles) and $T = 700$ °C (squares), as a function of $1/R$, displayed in a log-log scale. In both cases, ρ_{sl} decreases by a factor of ~ 2.5 upon increasing the growth rate from 0.036 to 0.370 nm/s. With the approximation above for $\tau_s = 1/R$, we would expect l_b^{sl} (or ρ_{sl}) $\sim R^{-1/3}$. A power fit of the data of Fig. 7(b) gives an exponent of -0.36 ± 0.05 for $T = 650$ °C and -0.32 ± 0.06 for $T = 700$ °C (see lines in the figure), showing that this simplifying interpretation of τ_s is able to explain quantitatively the observed dependence of ρ_{sl} on the growth rate.

D. Flattening of the profile in the absence of growth

To examine the thermal relaxation of the nonplanar surface profiles, we have compared the predictions of the model developed in Sec. III A for the bottom of the groove with a series of AlGaAs profiles, in which growth was interrupted for increasing time intervals after deposition of 100-nm-thick AlGaAs layers. This thickness is sufficient to ensure the achievement of a self-limiting profile in AlGaAs, just before the interruption.[9] Here 5-nm-thick GaAs marker layers were grown immediately after the growth interruptions, to quench and observe the relaxed AlGaAs profiles. Figure 8(a) shows the schematics of this layer sequence and TEM cross sections of two examples of such studies: namely, $Al_{0.45}Ga_{0.55}As$ layers grown at 700 °C without (top) and with (bottom) a 1800 s growth interruption before the marker layers. The widening of the profile due to the growth interruption is evident. In Fig. 8(b), we plot the bottom curvature $\kappa = 1/\rho$ of the $Al_{0.45}Ga_{0.55}As$ profile for $T = 700$ °C (circles) and 750 °C (squares), as a function of the growth interruption time t, in a log-log scale. For both temperatures, κ decreases by about a factor of 3, while t increases from 0 to 1800 s.

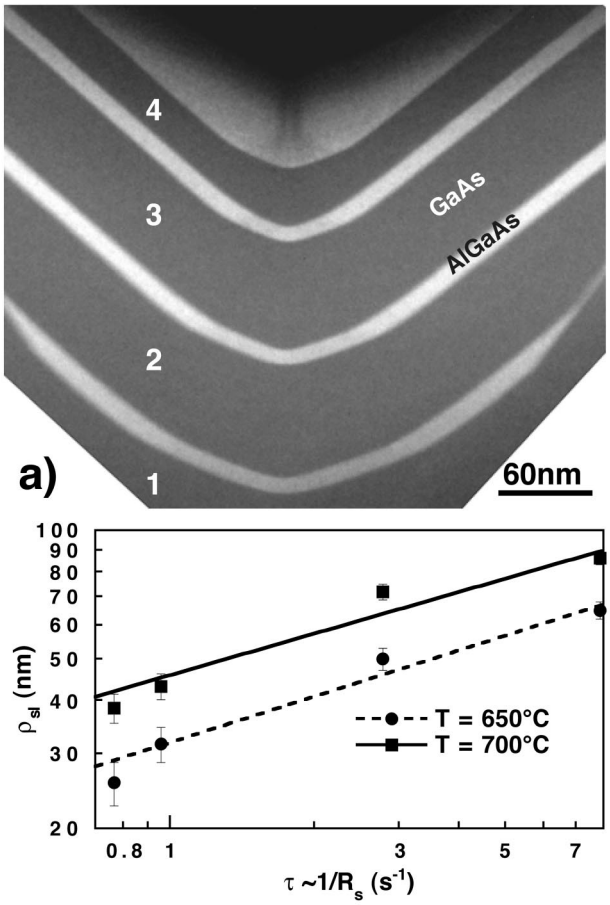

FIG. 7. (a) Dark-field TEM cross section of four GaAs layers, separated by AlGaAs markers and grown at 650 °C. The nominal growth rates were 0.036 nm/s (layer 1), 0.102 nm/ (2), 0.295 nm/ (3), and 0.370 nm/ (4), and the nominal thicknesses ranged between 25 and 50 nm. (b) Log-log plot of ρ_{sl} in GaAs layers, as a function of the inverse of the growth rate, for $T = 650$ °C (circles) and 700 °C (squares). Lines are power fits to the data (see text).

The curvature κ should tend to zero following the law

$$\kappa = \frac{\kappa_0}{(1 + t/\tau_b)^{\alpha}}, \tag{20}$$

where $\alpha = 0.25$, according to Eq. (12). The log-log plot evidences the $t^{-\alpha}$ dependence of the curvature, for $t/\tau_b \gg 1$. The solid and dashed lines are a fit of the data for 700 and 750 °C, respectively, with the function (20), in which the fit parameters are τ_b and α, while κ_0 (self-limiting curvature for the given x and T) is taken as the measured value of κ for $t = 0$. The fit to the two series of data yields values of 0.28 ± 0.02 and 0.27 ± 0.02 for α and 39 ± 10 s and 33 ± 5 s for

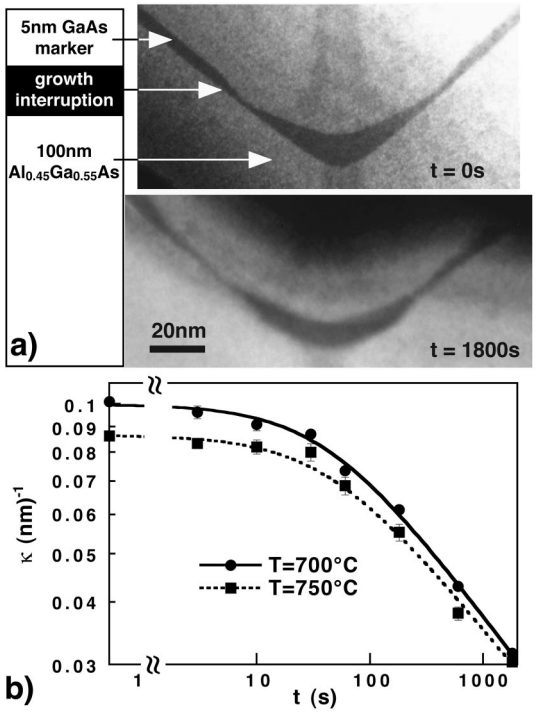

FIG. 8. (a) Left: schematics of the layer sequence used for the growth interruption studies. Right: TEM cross sections of the profiles at the bottom of the groove for a growth interruption of 0 s (top) and 1800 s (bottom), after growth of a 100-nm-thick $Al_{0.45}Ga_{0.55}As$ layer at 700 °C. (b) Self-limiting curvature $\kappa = 1/\rho$ at the bottom of a V groove in $Al_{0.45}Ga_{0.55}As$ alloys, as a function of the growth interruption time, for $T = 700$ °C (circles) and 750 °C (squares). Solid and dashed lines are fits of the experimental data with the function (20). The exponent appearing in Eq. (20) is a parameter of the fit.

τ_b, at $T = 700$ and 750 °C, respectively. The good match of the value of a with the theoretical value 0.25 demonstrates the validity of the model and of the simplifications assumed. The possible slight decrease of the recovery time τ_b with T can be associated with the Arrhenius dependence on T of n, which is the main quantity influencing the temperature behavior of τ_b, through relations (11) and (12).

E. Evolution of GaAs and $Al_xGa_{1-x}As$ profiles

We have compared the calculated and the experimental results for the time evolution of l_b towards its self-limiting value for GaAs, $Al_{0.3}Ga_{0.7}As$, and $Al_{0.45}Ga_{0.55}As$, grown at 650 and 700 °C. The samples consisted of a sequence of layers of increasing thickness, up to a thickness for which a self-limiting profile is established (about 50 nm). GaAs layers were grown on self-limiting $Al_xGa_{1-x}As$ profiles, and $Al_xGa_{1-x}As$ layers were grown on self-limiting GaAs profiles.

Figure 9(a) shows l_b, as a function of Z_n, for GaAs grown at 650 °C on self-limiting $Al_{0.3}Ga_{0.7}As$ (circles) and at 700 °C on self-limiting $Al_{0.45}Ga_{0.55}As$ (squares). Both profiles evolve towards their self-limiting sizes as the GaAs

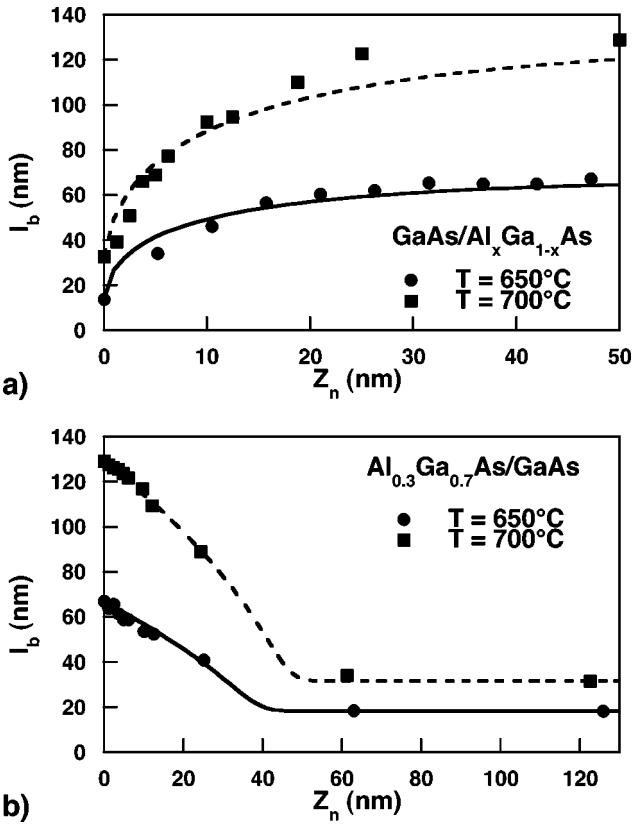

FIG. 9. (a) Measured evolution of the GaAs profile widths l_b towards their self-limiting value l_b^{sl} as a function of the nominal thickness, for $T = 650$ °C, grown on $Al_{0.45}Ga_{0.55}As$ (circles), and $T = 700$ °C, grown on $Al_{0.3}Ga_{0.7}As$ (squares). Solid lines are theoretical predictions of the profile evolutions [Eq. (16a)], with the parameters l_b^{sl} and Δr fixed as the values determined experimentally (see text). (b) Measured evolution of the $Al_{0.3}Ga_{0.7}As$ profile widths l_b towards their self-limiting value as a function of the nominal thickness, for $T = 650$ °C (circles) and $T = 700$ °C (squares), both grown on self-limiting GaAs. Solid lines are fits of the data, with the parameters l_b^{sl} and $\Delta r(x)$ fixed as the values determined experimentally and the Ga diffusion length on the sidewalls as a fitting parameter (see text).

thickness increases (see Table I). The time evolution of the GaAs profile has been modeled by integrating numerically Eq. (16a). The solid line represents the simulated profile evolution according to this equation, where we have selected the values of l_b^{sl} and Δr measured experimentally (see Table I). The evolutions of both GaAs profiles are well reproduced by the theoretical curves with our choice of parameters.

TABLE I. Measured self-limiting extensions of the bottom profiles and growth rate anisotropies Δr in GaAs, $Al_{0.3}Ga_{0.7}As$ and $Al_{0.45}Ga_{0.55}As$, grown at 650 and 700 °C.

x	l_b^{sl} (nm)		Δr	
	$T = 650$ °C	$T = 700$ °C	$T = 650$ °C	$T = 700$ °C
0	67±2	129±3	0.21±0.05	0.22±0.05
0.3	18.1±0.4	31.5±0.7	0.23±0.05	0.19±0.05
0.45	13.6±0.3	17.7±0.4	0.23±0.05	0.21±0.05

The self-limiting evolution of $Al_{0.3}Ga_{0.7}As$ and $Al_{0.45}Ga_{0.55}As$ (including entropy of mixing effects) is modeled by integrating numerically Eq. (18b). We have again plugged into the equation the measured values of the self-limiting profile widths and growth rate anisotropies (see Table I). We have left therefore L_s^G, contained in the parameter *b*, as a fitting parameter. Figure 9(b) shows the experimental points and the results of the fit for $Al_{0.3}Ga_{0.7}As$ at 650 °C (circles) and 700 °C (squares). A similar behavior is obtained for $Al_{0.45}Ga_{0.55}As$ (not shown). Least-squares fits of the experimental values at 700 °C yielded $L_s^G = 145 \pm 20$ nm from the $Al_{0.3}Ga_{0.7}As$ data and $L_s^G = 130 \pm 20$ nm from the $Al_{0.45}Ga_{0.55}As$ data. These values are consistent with each other and of the same order as those determined in Fig. 5(b), though about 20%–25% lower. At 650 °C, we obtained, consistently, $L_s^G = 90 \pm 10$ nm from the $Al_{0.3}Ga_{0.7}As$ data and $L_s^G = 70 \pm 10$ nm from the $Al_{0.45}Ga_{0.55}As$ data. The ratio between the average Ga diffusion lengths at 650 and 700 °C yields $L_s^G(650\,°C)/L_s^G(700°C) = 0.58 \pm 0.11$. Since $L_s = (D_s \tau_s)^{1/2}$ and $\tau_s \approx 1/R$, according to Eq. (19) we have

$$\frac{L_s^G(T_1)}{L_s^G(T_2)} = \exp\left[\frac{E_B^G}{2}\left(\frac{1}{k_B T_2} - \frac{1}{k_B T_1}\right)\right].$$

With $E_B^G = 1.9 \pm 0.3$ eV (see Sec. V B), this relation gives a diffusion length ratio $L_s{}^G(650°C)/L_s^G(700\,°C) = 0.55 \pm 0.11$, in excellent agreement with the value found from the fits above.

Figure 9 shows that the transient size variations taking place during evolution towards the self-limiting profile are qualitatively different, depending on whether $l_b^0 < l_b^{sl}$ (a) or $l_b^0 > l_b^{sl}$ (b).

GaAs/Al$_x$Ga$_{1-x}$As case (a). In the initial stages of profile evolution we have $l_b \ll l_b^{sl}$; therefore, the term "-1" can be neglected in Eq. (16a) and the profile will evolve approximately according to the law (12). This is due to the fact that, when the profile is very sharp, with respect to the surface diffusion length, lateral capillarity fluxes are dominant over nominal growth fluxes.

Al$_x$Ga$_{1-x}$As/GaAs case (b). In the initial stages of profile evolution, we have $l_b \gg l_b^{sl}$; therefore, the capillarity and entropy of mixing terms can be neglected in Eq. (18b). This is equivalent to stating that for very shallow profiles (much wider than the surface diffusion length), lateral fluxes are negligible, and each facet grows with its "intrinsic" growth rate r_i. As a consequence [see Eq. (18b)], the profile contraction is initially constant, at a rate given by $\Delta r(x)$. This linear profile evolution is well reproduced in Fig. 9(b) for $l_b \leqslant 20$ nm.

VI. FORMATION OF QUANTUM-CONFINED NANOSTRUCTURES

The model developed above is useful not only for evaluating the self-limiting characteristics of the growth, but can also be employed to elucidate the self-ordering of several types of quantum nanostructures relying on such self-limiting surface evolution.

A. Al$_x$Ga$_{1-x}$As VQW's

As seen above, the Ga segregation in the VQW's during AlGaAs growth derives directly from the higher mobility of Ga adatoms, with respect to the Al ones, and from the corrections due to entropy of mixing effects. The self-limiting facet widths for AlGaAs alloys give the confinement dimension of VQW structures. A detailed account of the formation mechanisms of such VQW's is given elsewhere.[30]

B. GaAs/Al$_x$Ga$_{1-x}$As QWR's

The fact that the self-limiting width increases with increasing diffusion length of the group-III adatoms on the sidewalls explains directly the self-ordering of crescent-shaped QWR's. Thus, growing a low-band-gap semiconductor layer (e.g., GaAs), characterized by a longer diffusion length, on a self-limiting, higher-band-gap V-groove surface (e.g., AlGaAs) leads to an expansion of the bottom facet and the experimentally observed formation of a QWR. The QWR shape can be predicted, as a function of the nominal GaAs thickness and growth conditions, using Eq. (16a). For the typical GaAs/AlGaAs QWR thicknesses, we have $l_b \ll l_b^{sl}$ (for GaAs); therefore, we can neglect the deposition term ("-1") in Eq. (16a) and approximate l_b with the analytic formula (12), with $\tau_b = (l_{b,AG}^{sl})^4/[4p\Delta r (l_{b,G}^{sl})^3]$ (where "*AG*" stands for AlGaAs). The thickness profile $t(X,Z_n)$, as a function of the lateral coordinate *X* and of the nominal thickness Z_n, can be easily found within the approximations taking into account a single bottom facet or a hyperbolic surface profile. In this latter case, $t(X,Z_n)$ becomes

$$t(X,Z_n) = r_s Z_n + \tan(\theta)\left[\sqrt{[\rho_0 \tan(\theta)]^2\left(1 + \frac{Z_n}{\tau_b}\right)^{1/2} + X^2} - \sqrt{[\rho_0 \tan(\theta)]^2 + X^2}\right], \quad (21)$$

where ρ_0 is the bottom radius of curvature on which the QWR is deposited and, in this case, corresponds to the AlGaAs self-limiting radius. This equation defines completely the QWR shape in the hyperbolic approximation, as a function of the material self-limiting shapes and of the nominal thickness.

As an example, we plot in Fig. 10(a) the thickness profile of a GaAs QWR with nominal thickness $Z_n = 2.5$ nm, with the self-limiting parameters measured experimentally: $\rho_{b,AG}^{sl} = 6.4$ nm (corresponding to an Al mole fraction $x = 0.4$ and a growth temperature $T = 650$ °C, with $R = 0.4$ nm/s) and $\rho_{b,G}^{sl} = 24$ nm ($x = 0$, $T = 650$ °C, $R = 0.25$ nm/s, solid line). For comparison, the figure also shows thickness profiles for the same $\rho_{b,AG}^{sl}$ and Z_n, with $\rho_{b,G}^{sl} = 12$ nm (dotted line) and $\rho_{b,G}^{sl} = 48$ nm (dash-dotted line).

The relation above can be used to calculate the wire quantum confinement potential. This can be done analytically in the adiabatic approximation for the case of an infinitely deep transverse potential well.[34] In this limit, the electron subband separation found in Ref. 34 can be expressed as

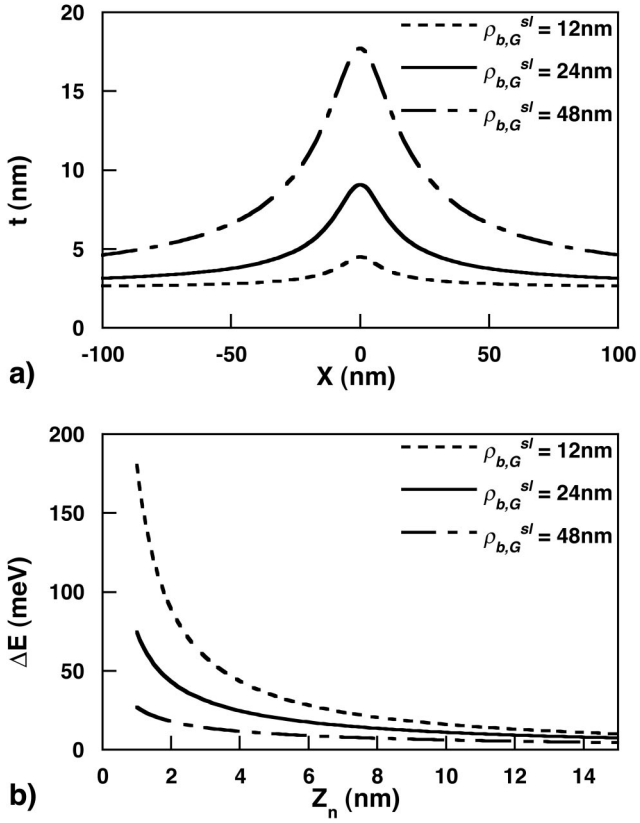

FIG. 10. (a) Simulated thickness profiles of a hyperbolic-shaped GaAs/AlGaAs QWR with nominal thickness 2.5 nm, $\rho_{b,AG}^{sl}=6.4$ nm, and $\rho_{b,G}^{sl}=12$ nm (dotted line), 24 nm (solid line), and 48 nm (dashed-dotted line). (b) Calculated electron subband separation energies, as a function of the nominal QWR thickness, for the three sets of growth parameters of part (a), in the adiabatic approximation, for an infinitely deep transverse potential well (Ref. 34).

$$\Delta E=\frac{\hbar^2\pi}{m^*}\sqrt{\frac{1-(1+Z_n/\tau_b)^{-1/4}}{\rho_{b,AG}^{sl}t(0,Z_n)^3}},$$

where m^* is the electron effective mass and $t(0,Z_n)$ is the GaAs layer thickness at the bottom of the QWR crescent, calculated from Eq. (21). The calculated values of ΔE as a function of the nominal thickness, for the sets of parameters of the three QWR profiles considered above, are plotted in Fig. 10(b).

C. GaAs/Al_xGa_{1-x}As QWR superlattices

We have shown in Ref. 37 that GaAs/Al_xGa_{1-x}As QWR superlattices can be grown with Al_xGa_{1-x}As barriers much thinner than the ones needed to recover the self-limiting Al_xGa_{1-x}As profile. A peculiar SL self-limiting state is established and has been modeled analytically in Ref. 37 by using empirical, exponential evolution laws for the GaAs and Al_xGa_{1-x}As profiles. In Fig. 11 we show the measured GaAs and Al_xGa_{1-x}As radii of curvature, as a function of thickness, in a (1.8 nm/3.9 nm) GaAs/$Al_{0.45}Ga_{0.55}$As SL grown at 650 °C (open symbols). It can be seen that, after an initial transient, the profile variations during deposition of a single

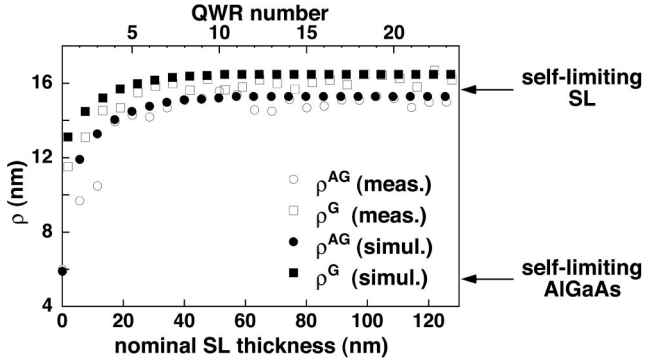

FIG. 11. Open symbols: measured QWR SL radius of curvature, as a function of the SL thickness, in a (1.8 nm/3.9 nm) GaAs/$Al_{0.45}Ga_{0.55}$As SL grown at 650 °C. Solid symbols: simulated radius of curvature, using Eqs. (16a) and (18b). Circles: upper $Al_{0.45}Ga_{0.55}$As profile. Squares: upper GaAs profile.

layer balance themselves over each period, thus yielding a self-limiting SL evolution. Solid symbols show the result of the modeling of SL growth, where we have simulated numerically the SL profile using Eqs. (16a) and (18b). The parameters of the simulation were fixed by fitting the self-limiting evolution of GaAs and $Al_{0.45}Ga_{0.55}$As at 650 °C, determined in Sec. V E. The plot shows that the SL self-limiting growth can be well reproduced with our model. The simulation gave self-limiting SL radii of curvature of 17.9 nm, 15.9 nm, 13.4 nm, and 12.0 nm for SL's with $Al_{0.45}Ga_{0.55}$As thicknesses of 2.2 nm, 3.9 nm, 7.8 nm, and 11.6 nm, respectively. The agreement with the experimental values (19.1 ± 1.1 nm, 15.6 ± 0.3 nm, 12.9 ± 0.5 nm, and 11.0 ± 0.7 nm, respectively) is comparable to that of the empirical model presented in Ref. 37, based on the exponential evolution of GaAs and AlGaAs profiles.

D. $In_xGa_{1-x}As/Al_xGa_{1-x}As$ QWR's

Compositional self-ordering takes place also in $In_xGa_{1-x}As$ alloy layers grown on V grooves, resulting in the formation of an In-rich VQW at the bottom of the groove.[38] InGaAs self-ordering can be explained by our model, as the diffusion length of In is larger than that of Ga. In this case, however, one should also take into account the effects of strain when InGaAs is grown on GaAs or AlGaAs buffer layers. This can be done formally by solving the Nernst-Einstein and continuity equations outlined above, with a surface chemical potential that takes into account nonplanarity, entropy of mixing, *and* strain, this latter effect being included through Eq. (1). Besides this complication, experimental determination of the structural parameters in these systems is less straightforward than in the $Al_xGa_{1-x}As$/GaAs case, since the contrast obtained in AFM (Ref. 39) and dark-field TEM cross sections is due both to composition and strain. Some complementary information is therefore needed, such as, for example, the lateral and vertical strain distributions that can be inferred from high-resolution x-ray diffraction.[40–42]

E. $Al_xGa_{1-x}As/GaAs$ quantum dots on inverted pyramids

By etching tetrahedral recesses on (111)*B*-oriented GaAs substrates, self-ordering of OMCVD-grown $Al_xGa_{1-x}As$ is observed at the bottom of these pyramids.[13] Growth on the side facets of the pyramids is analogous to the one taking place in V grooves: sidewalls with similar quasi-{111}*A* planes develop, and at their intersection self-ordered $GaAs/Al_xGa_{1-x}As$ QWR's and $Al_xGa_{1-x}As$ VQW's are formed.[13] At the bottom of the pyramids, at the intersection of the three QWR's and VQW's, a GaAs quantum dot and a vertical AlGaAs QWR form, respectively.[13] Our model can be extended to treat two-dimensional lateral diffusion in such a tetrahedral geometry.

F. Conclusions

In summary, we have developed an analytic model that explains self-ordered epitaxy on nonplanar substrates. Self-limiting profiles result from the interplay among three processes.

(i) The *growth rate anisotropy* among the different facets composing the grooved profile. This anisotropy depends on the growth technique and leads to a resharpening of the nonplanar profile either at the bottom of the grooves (typically in OMCVD on $[01\bar{1}]$-oriented grooves) or at the top of the ridge (typically in MBE on [011]-oriented grooves).

(ii) The *capillarity fluxes* of adatoms towards the bottom of the groove. These fluxes can self-adjust in order to yield a steady-state propagation of the faceted profile either at the bottom or at the top region, depending on the growth rate anisotropy. The dependence of these fluxes on the adatom diffusion length determines the self-limiting profile width, as a function of the material and growth conditions.

(iii) The nonuniformity of the *entropy of mixing* in the profile of alloys. The different diffusion length of the alloy components results in segregation of the more mobile species at the bottom of the groove and of the less mobile at the top of the mesa. However, these variations of the alloy composition give rise to gradients of the entropy of mixing, which tend to reestablish a uniform composition.

With suitable approximations, we were able to apply quantitatively our model to the experimental self-limiting behavior of $GaAs/Al_xGa_{1-x}As$ nanostructures grown by LP OMCVD on V-grooved substrates. Besides giving an accurate physical interpretation of self-ordering phenomena in nonplanar epitaxy, this analytic model provides an estimate of some quantities relevant to the epitaxial process, such as adatom diffusion lengths and activation energies on the groove sidewalls.

Our model could be further developed in the future to describe the self-limiting growth of more complex systems. By including the effects of strain on the surface chemical potential, the model could be extended to lattice-mismatched $In_xGa_{1-x}As/(Al)GaAs$ heteroepitaxy on V grooves,[38] provided that a more detailed knowledge of the composition and strain profiles in these structures can be obtained. Finally, by formulating the corresponding two-dimensional diffusion process, it should be possible to describe self-limiting growth of GaAs/AlGaAs quantum dots grown on (111)*B*-patterned substrates, where the dots form at the intersection of three planes at the bottom of a tetrahedral inverted pyramid.[13]

APPENDIX

In this paper, we have developed a diffusion model to explain self-limiting growth at the bottom of the grooves by assuming that this region is composed only of a single facet. This simplification has proved to be very useful for interpreting self-ordering phenomena as a function of a few physical parameters, which can be easily inferred from experimental results. This picture, however, lacks a description of the full fine structure of the extremal regions. In this appendix we will present the equations of motion for all three facets [one central (100) and two lateral {311}*A*] that constitute the extremal regions, again fixing our attention to the bottom of the groove (see Fig. 2).

For such a structure, the chemical potential at each facet is given by the set of equations

$$\mu_{1t}=\mu_0+\frac{\bar{\gamma}_1\Omega_0}{l_{1t}},$$

$$\mu_{3t}=\mu_0+\frac{\bar{\gamma}_3\Omega_0}{l_{3t}},$$

$$\mu_s=\mu_0,$$

$$\mu_{3b}=\mu_0-\frac{\bar{\gamma}_3\Omega_0}{l_{3b}},$$

$$\mu_{1b}=\mu_0-\frac{\bar{\gamma}_1\Omega_0}{l_{1b}},$$

where

$$\bar{\gamma}_1=2(\gamma_3\csc\alpha-\gamma_1\cot\alpha),$$

$$\bar{\gamma}_3=\gamma_s\csc(\theta-\alpha)+\gamma_1\csc\alpha-\gamma_3(\cot(\theta-\alpha)+\cot\alpha),$$

α is the angle between the {311}*A* and the (100) facets (see Fig. 2), and the subscripts 1 and 3 refer to the (100) and {311}*A* facets, respectively. According to Eq. (6), therefore, the surface fluxes between the sidewalls and the bottom {311}*A* and between the bottom {311}*A* and the bottom (100) are, respectively,

$$j_{3b}=\frac{n_{3s}D_s\Omega_0\bar{\gamma}_3}{k_BTl_{3b}^2},$$

$$j_{1b}=\frac{n_{13}D_3\Omega_0}{k_BTl_{1b}^2}\left(\frac{\bar{\gamma}_1}{l_{1b}}-\frac{\bar{\gamma}_3}{l_{3b}}\right).$$

We will assume that the boundaries between the {311}*A* and the sidewalls evolve also in this case according to Eq. (16a), with $l_b=2l_{3b}\cos\alpha+l_{1b}$. This assumption is justified by the good agreement of the observed behavior of l_b with

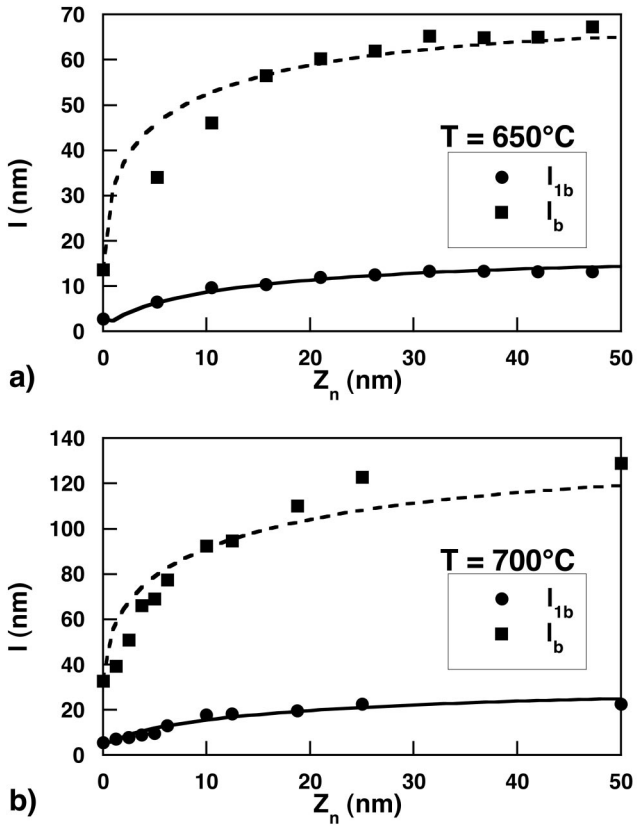

FIG. 12. Measured (symbols) and calculated (lines) evolution of the (100) (circles) and {311}*A* (squares) boundaries in GaAs heteroepitaxy on self-limiting $Al_{0.45}Ga_{0.55}As$ at 650 °C (a) and on self-limiting $Al_{0.3}Ga_{0.7}As$ at 700 °C (b).

the simplified model developed above. According to Eq. (8), the equation of motion of the central (100) facet can be written as

$$\frac{dZ_{1b}}{dt}=R_1+\frac{2\Omega_0}{l_{1b}}j_{1b}.$$

The adatom concentration n_{13} at the boundaries between the bottom {311}*A* and (100) can be found as mentioned in Sec. III B. After some algebra, we obtain

$$n_{13}=\frac{R_3}{\Omega_0}\frac{l_{3b}}{K_{1b}+K_{3b}},$$

where the atom transfer rates $K_{1b}=j_{1b}/n_{13}$ and $K_{3b}=j_{3b}/n_{3s}$ are independent of the adatom concentrations. By noticing that $dl_{1b}=(2\cot\alpha)(dZ_{1b}-dZ_{3b})$, we obtain

$$\frac{dl_{1b}}{dZ_n}=2\cot\alpha\left[r_1+r_3\left(2\frac{l_{3b}^3}{Al_{1b}^3+l_{1b}l_{3b}^2}E\right)\right],$$

where $A=(D_s/D_3)(\overline{\gamma_3}/\overline{\gamma_1})$. The equation above and Eq. (16a) define the evolution of the {311}*A* and (100) boundaries, in the absence of the entropy of mixing effects.

We have fitted the evolution of l_{1b} and l_b for GaAs profiles, at $T=650$ and 700 °C [see Fig. 9(a)] with the system of equations just described. In Fig. 12 we show the results of such fits, where we have fixed the r_i's to their measured values and varied the parameter *A*. A good match to the experimental data is obtained for $A\approx 5-10$ for the two cases described here. Since *A* is the ratio of quantities that should not differ significantly from facet to facet, it is reasonable to obtain values for *A* not too far from 1. Thus, the results support the validity of the procedure and of the approximations made above. However, we will not discuss further the numerical value of *A* found here, since it is not possible to estimate independently the diffusion coefficient and surface energy ratios that appear in this parameter.

ACKNOWLEDGMENTS

This work was partially supported by the Fonds National Suisse de la Recherche Scientifique. We thank Francois Lelarge for useful discussions and Adriana Condo for performing transmission electron microscopy.

*Present address: Laboratorio Nazionale TASC-INFM, S.S. 14, Km 163.5 Basovizza, I-34012 Trieste, Italy. Electronic address: biasiol@tasc.infm.it

[1] E. Kapon, Semicond. Semimetals **40**, 259 (1994).
[2] K. Kash, A. Scherer, J.M. Worlok, H.G. Craighead, and M.C. Tamargo, Appl. Phys. Lett. **49**, 1043 (1986).
[3] J.Y. Marzin, A. Izrael, L. Birotheau, B. Sermage, N. Roy, R. Azoulay, D. Robein, J.-L. Benchimol, L. Henry, V. Thierry-Mieg, F.R. Ladan, and L. Taylor, Surf. Sci. **267**, 253 (1992).
[4] M. Tsuchiya, J.M. Gaines, R.H. Yan, R.J. Simes, P.O. Holtz, L.A. Coldren, and P.M. Petroff, Phys. Rev. Lett. **62**, 466 (1989).
[5] H. Drexler, D. Leonard, W. Hansen, J.P. Kotthaus, and P.M. Petroff, Phys. Rev. Lett. **73**, 2252 (1994).
[6] Q. Xie, A. Madhukar, P. Chen, and N.P. Kobayashi, Phys. Rev. Lett. **75**, 2542 (1995).
[7] E. Kapon, D.M. Hwang, and R. Bhat, Phys. Rev. Lett. **63**, 430 (1989).
[8] G. Vermeire, I. Moerman, Z.Q. Yu, F. Vermaerke, P. Van Daele, and P. Demeester, J. Electron. Mater. **23**, 121 (1994).
[9] A. Gustafsson, F. Reinhardt, G. Biasiol, and E. Kapon, Appl. Phys. Lett. **67**, 3673 (1995).
[10] X.-L. Wang, M. Ogura, and H. Matsuhata, Appl. Phys. Lett. **66**, 1506 (1995).
[11] A. Hartmann, M. Bongartz, M. Hollfelder, H. Hardtdegen, C. Dieker, and H. Luth, J. Cryst. Growth **170**, 605 (1997).
[12] S. Koshiba, H. Noge, H. Akiyama, T. Inoshita, Y. Nakamura, A. Shimizu, Y. Nagamune, M. Tsuchiya, H. Kano, H. Sakaki, and K. Wada, Appl. Phys. Lett. **64**, 363 (1994).
[13] A. Hartmann, L. Loubies, F. Reinhardt, and E. Kapon, Appl. Phys. Lett. **71**, 1314 (1997).
[14] S. Ishida, Y. Arakawa, and K. Wada, Appl. Phys. Lett. **72**, 800 (1998).
[15] K. Yamaguchi and K. Okamoto, Appl. Phys. Lett. **59**, 3580 (1991).
[16] S. Koshiba, T. Noda, H. Noge, Y. Nakamura, H. Ichinose, T. Shitara, D.D. Vvedensky, and H. Sakaki, J. Cryst. Growth **150**, 322 (1995).

[17] S.D. Hersee, E. Barbier, and R. Blondeau, J. Cryst. Growth **77**, 310 (1986); K.M. Dzurko, S.G. Hummell, E.P. Menu, and P.D. Dapkus, J. Electron. Mater. **19**, 1367 (1990); D.G. Coronell and K.F. Jensen, J. Cryst. Growth **114**, 581 (1991); Y. Ueta, N. Wada, S. Sakai, and Y. Shintani, J. Electron. Mater. **21**, 355 (1992); S.H. Jones and L.S. Salinas, J. Cryst. Growth **154**, 163 (1995).

[18] M. Hata, T. Isu, A. Watanabe, and Y. Katayama, J. Vac. Sci. Technol. B **8**, 692 (1990); X.Q. Shen, D. Kishimoto, and T. Nishinaga, Jpn. J. Appl. Phys., Part 1 **33**, 11 (1994); S. Koshiba, Y. Nakamura, M. Tsuchiya, H. Noge, H. Kano, Y. Nagamune, T. Noda, and H. Sakaki, J. Appl. Phys. **76**, 4138 (1994).

[19] W.W. Mullins, J. Appl. Phys. **28**, 333 (1957).

[20] J. Y. Tsao, *Material Fundamentals of Molecular Beam Epitaxy* (Academic, Boston, 1993).

[21] G. Biasiol and E. Kapon, Phys. Rev. Lett. **81**, 2962 (1998).

[22] Strictly speaking, one should take into account surface stresses as well, in addition to surface energy, in calculating the chemical potential related to surface nonplanarities. However, stress-related contributions can be neglected for surface curvatures typical of our nonplanar epitaxy and should emerge only when sharper features are formed (see, for example, Refs. 43 and 44).

[23] C. Herring, in *The Physics of Powder Metallurgy*, edited by W. E. Kingston (McGraw-Hill, New York, 1951), pp. 143–179.

[24] E. Adam, A. Chame, F. Lancon, and J. Villain, J. Phys. I **7**, 1455 (1997) and references therein.

[25] X.Q. Shen, M. Tanaka, K. Wada, and T. Nishinaga, J. Cryst. Growth **135**, 85 (1994).

[26] M. Ozdemir and A. Zangwill, J. Vac. Sci. Technol. A **10**, 684 (1992).

[27] We will refer all our space-dependent variables (growth rates, surface densities, diffusion lengths, constants, etc.) and derivatives to a Cartesian system with vertical and horizontal coordinates, except otherwise indicated. Values along a facet or a facet normal can be found by scaling by the cosine of the angle that the facet forms with the horizontal.

[28] G. Biasiol, F. Reinhardt, A. Gustafsson, E. Martinet, and E. Kapon, Appl. Phys. Lett. **69**, 2710 (1996).

[29] A. Kley, P. Ruggerone, and M. Scheffler, Phys. Rev. Lett. **79**, 5278 (1997), and references therein.

[30] G. Biasiol, K. Leifer, A. Gustafsson, and E. Kapon (unpublished).

[31] T. Kono, S. Tsukamoto, Y. Nagamune, F. Sogawa, M. Nishioka, and Y. Arakawa, Appl. Phys. Lett. **64**, 1564 (1994).

[32] This can be effectively considered as the upper limit for the migrating adatom lifetime τ_s (Ref. 45). This time is in general lower than $1/R$, since an adatom could reevaporate before the arrival of another adatom at the same site (Ref. 46); however, no appreciable group-III adatom reevaporation is observed for our growth conditions.

[33] We will neglect a weak dependence on T coming from the factor $(k_B T)^{-1/3}$ and from the pre-exponential factor of the diffusion coefficient D_{s0}. This latter one, in particular, is considered to be virtually temperature independent, as compared with the exponential term [J. Villain and A. Pimpinelli, *Physique de la croissance cristalline* (Ed. Eyrolles, Collection Aléa Saclay, Paris, 1995)].

[34] E. Kapon, G. Biasiol, D.M. Hwang, M. Walther, and E. Colas, Solid-State Electron. **40**, 1 (1996).

[35] N. Moll, A. Kley, E. Pehlke, and M. Scheffler, Phys. Rev. B **54**, 8844 (1996).

[36] G. Biasiol, F. Reinhardt, A. Gustafsson, and E. Kapon, Appl. Phys. Lett. **71**, 1831 (1997).

[37] G. Biasiol, E. Kapon, Y. Ducommun, and A. Gustafsson, Phys. Rev. B **57**, R9416 (1998).

[38] G. Biasiol, F. Reinhardt, A. Gustafsson, and E. Kapon, J. Electron. Mater. **26**, 1194 (1997).

[39] F. Reinhardt, B. Dwir, G. Biasiol, and E. Kapon, Appl. Surf. Sci. **104**, 529 (1996).

[40] Q. Shen, S.W. Kycia, E.S. Tentarelli, W.J. Schaff, and L.F. Eastman, Phys. Rev. B **54**, 16 381 (1996).

[41] L. Leprince, G.T. Baumbach, A. Talneau, M. Gailhanou, and J. Schneck, Appl. Phys. Lett. **71**, 3227 (1997).

[42] N. Darowski, U. Pietsch, U. Zeimer, V. Smirnitzki, and F. Bugge, J. Appl. Phys. **84**, 1366 (1998).

[43] C. Herring, in *Structure and Properties of Solid Surfaces*, edited by R. Gomer and C. S. Smith (The University of Chicago Press, Chicago, 1953), pp. 5–81.

[44] V.I. Marchenko and A.Ya. Parshin, Sov. Phys. JETP **52**, 129 (1980).

[45] J.D. Weeks and G.H. Gilmer, Adv. Chem. Phys. **40**, 157 (1979).

[46] T. Nishinaga, in *Handbook of Crystal Growth*, edited by D. T. J. Hurle (North-Holland, Amsterdam, 1994), Vol. 3b, p. 665.